# Exploiting the impact of Ionic Liquids and light exposure on performance of fully inorganic CsPbBr3 semi-transparent perovskite solar cells

Jessica Barichello, Barbara Paci, Paolo Moras, Javid Hajhemati, Amanda Generosi, Flavia Righi Riva, Stefania Cacovich, Farshad Jafarzadeh, Francesca Brunetti, Aldo Di Carlo, et al.

# Exploiting the impact of Ionic Liquids and light exposure on performance of fully inorganic $CsPbBr_3$ semi-transparent perovskite solar cells

Jessica Barichello[a], Barbara Paci[a], Paolo Moras[b], Javid Hajhemati[d], Amanda Generosi[a], Flavia Righi Riva[a], Stefania Cacovich[d], Farshad Jafarzadeh[c], Francesca Brunetti[c], Aldo Di Carlo[a,c], Fabio Matteocci[c*]

[a]CNR-Istituto di Struttura della Materia (CNR-ISM), Via del Fosso del Cavaliere 100, 00133, Roma, Italy

[b] CNR-Istituto di Struttura della Materia (CNR-ISM), SS 14, Km 163.5, 34149 Trieste, Italy

[c]CHOSE, Centre for Hybrid Organic Solar Energy, Department of Electronic Engineering, University of Rome, Tor Vergata, Via del Politecnico 1, 000133, Roma, Italy

[d] Institut Photovoltaïque d'Ile-de-France (IPVF), UMR 9006, CNRS, Ecole Polytechnique, IP Paris, Chimie Paristech, PSL, 91120 Palaiseau, France

*corresponding author: mailto:

## Abstract

Inorganic wide-bandgap $CsPbBr_3$ perovskite is an interesting material to investigate for several opto-electronic devices such as solar cells, detectors and light emitting diodes. Although the 2.3eV-bandgap limits the achievement of power conversion efficiencies (PCEs) larger than 10% in opaque perovskite solar cells (PSC), these materials are still interesting in several photovoltaic (PV) fields, such as Building Integrated PV and agri-PV, where the semi-transparency of the device stack can represent an additional value. However, the single-step solution processing is challenging due to the limited solubility of the precursors. Although sequential deposition of $PbBr_2$ and CsBr could mitigate this issue, further concerns occurred on the achievement of pure α-phase $CsPbBr_3$ thin film. In this work, we developed a deposition process where the use of BMIM-$BF_4$ ionic liquid in $PbBr_2$ deposition helps the formation of $CsPbBr_3$ with improved uniformity and reduced presence of competitive perovskite phases. Thanks to the ionic liquid addition, the PCE was drastically improved up to 6.33% on semi-transparent PSCs using sputtered Indium Tin Oxide as transparent top contact. The Average Visible Transmittance of the full device stack exceeded 58% with Light Utilization Efficiency greater than 3.67%. Finally, we investigated thank to photoemission spectroscopy and in-situ XRD analysis the impact of the light exposure in the bulk and/or at the surface of thin film.

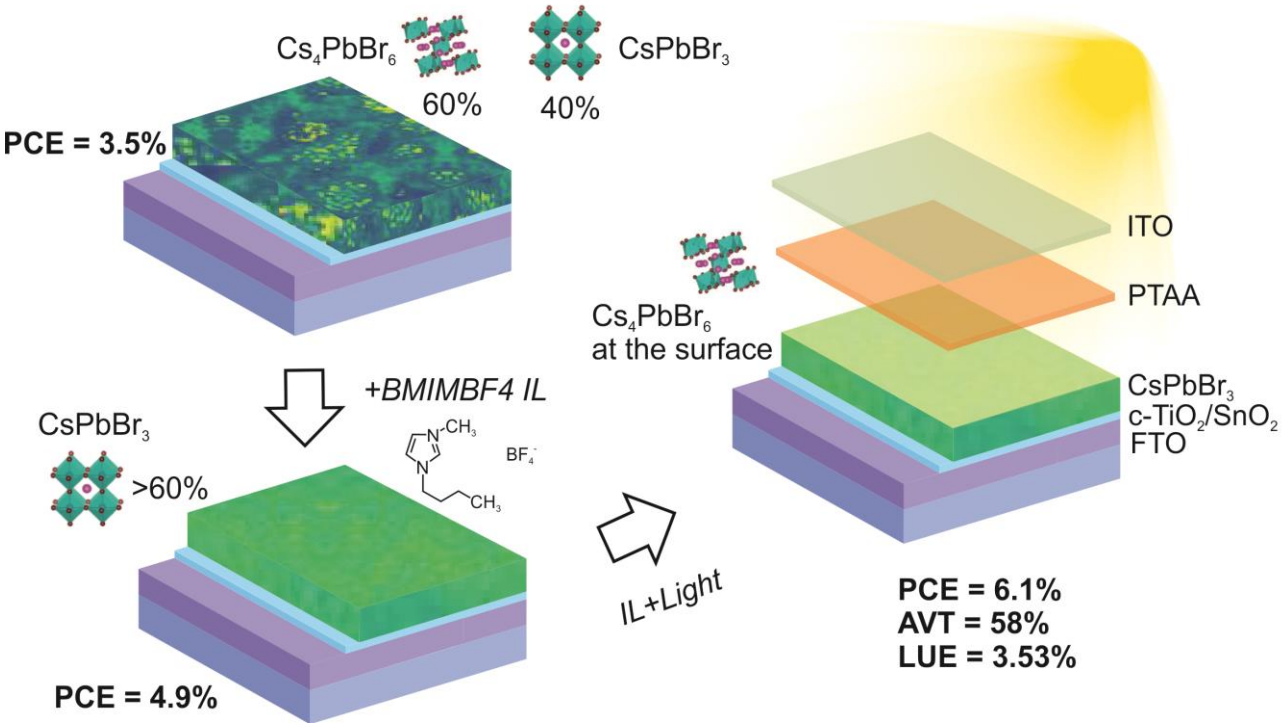


## Introduction

Perovskite Solar Cells (PSCs) have been considered the most promising third-generation thin film photovoltaic (PV) technology due to their impressive power conversion efficiency (PCE) of up to 26.2%[1]. Currently, lead halide perovskites are the most used perovskite compounds for photovoltaic application where fully iodide composition leads in terms of achieved PCEs due to the optimal bandgap for visible light absorption[2-5]. Generally, the most efficient single-junction devices have been fabricated on opaque device stack by solution processing or physical methods limiting their use in fields where semi-transparency play a role like multi-junction tandems[6-8] and transparent PV (TPV) for BIPV[9-11]. In BIPV field, Traverse et al. described the potential of TPV when integrated as building elements (mainly facades and smart windows) showing that an Average Visible Transmittance (AVT) greater than 30% is required for a feasible BIPV application[12]. In this scenario, semi-transparent perovskite solar cells (ST-PSCs) can play in the game only if the perovskite thin film shows specific features in terms of thickness and bandgap[13-15]. In our recent publications, we demonstrated that hybrid lead bromide and bromide/chloride perovskite compounds can be used as light absorber with relatively high transmission in the visible spectrum[16-20]. Our best ST-PSC showed PCE greater than 8% with AVT up to 70% for a record Light Utilization Efficiency (LUE) of 5.72%[20]. Organic cations (FA and MA) can be replaced with inorganic counterpart such as Cs in order to obtain $CsPbX_3$ inorganic halide bromide perovskites where X is an halogen (I, Br,Cl)[21]. In literature, $CsPbBr_3$ having

direct bandgap at 2.3eV is deeply investigated for solar cells, light emitting diodes and x-ray detectors for its excellent stability under heat and moisture stresses[22-24]. However, $CsPbBr_3$ also has two derivative phases: $CsPb_2Br_5$ and $Cs_4PbBr_6$[25]. The former exhibits a two-dimensional layer structure, while the latter shows a 0-D structure based on $[PbBr]^{4-}$ octahedra disconnected from each other by CsBr bridges due to abundant CsBr. Recently, several research groups have investigated the PV properties of $CsPbBr_3$ in solar cells using different deposition approaches. Regarding solution processing, sequential deposition process is preferred to single-step due to the limited solubility of CsBr precursor in common solvents such as N,N-dimetilformammide (DMF) and Dimethylsufoxide (DMSO)[26]. In sequential deposition, CsBr is often deposited using multiple spin coating steps in order to obtain the final conversion in $CsPbBr_3$ avoiding the presence of unconverted $PbBr_2$[27] . This solution clearly limits future development of an up-scaling scaling process. To solve this issue, Cao et al. introduced a second step process where CsBr is dissolved in not-harmful mixture of water/ethanol reaching 6.12% PCE in opaque cells[28]. The PCEs up to 10.9% have been reached on opaque device stack using carbon[29, 30], gold[31], or silver[32] as top electrodes. However, it hinders their application in several fields where the device transparency plays a crucial role such as multi-junction solar cells and BIPV. Recently, Jiang et al. demonstrate the development of ST-PSC based on fully evaporated $CsPbBr_3$ with thickness of 500nm reaching a maximum PCE of 7.28% and AVT of 44.2% using Indium Tin Oxide (ITO) as transparent top electrode[33].

In this paper, we investigated the development of fully-solution processed $CsPbBr_3$ made by sequential process using a modified $PbBr_2$ process followed by single-step CsBr spin coating for final perovskite conversion able to fabricate efficient ST-PSCs. In literature, several kinds of ionic liquids have been utilized for improving the film morphology and crystallinity of the perovskite absorber[34]. Zhang et al. incorporate a thin layer of IL, 1-butyl-2,3-dimethylimidazolium chloride ([BMMIm]Cl) on top of a carbon-based $CsPbBr_3$ perovskite to passivate defects and enhance the energy-level alignment at the perovskite/carbon interface[35]. This resulted in improved device performance, mainly attributed to the passivation of unsaturated $Pb^{2+}$ and $Cs^{+}$ ions on the surface of the photoactive layer and the minimization of the interface energy-level difference. With this aim, we further investigated the beneficial role of ionic liquids (ILs) during the $CsPbBr_3$ deposition made by sequential deposition process. Here, we included low content of 1-Butyl-3-methylimidazolium tetrafluoroborate (BMIM-BF4)-IL in $PbBr_2$ solution for evaluating the impact on structural and morphological properties of the resulting $CsPbBr_3$ perovskite layer thanks to X-Ray Diffraction (XRD) and Photo-Emission Spectroscopy (PES) characterization. The results indicate the beneficial role of BMIM-$BF_4$ IL on the formation of $CsPbBr_3$ phase with reduced content of competitive $Cs_4PbBr_6$ phase. Moreover, hyperspectral photoluminescence imaging revealed better uniformity of the perovskite with peaked emission at 2.3eV. Furthermore, we evaluated sputtered ITO as transparent top electrode to exploit

the feasibility of $CsPbBr_3$-based semi-transparent PSCs for Building Integrated Photovoltaics or IoT applications meeting a compromise between transparency and efficiency with a deposited thin layer of perovskite. Furthermore, we investigated how the light soaking at Maximum Power Point Tracking (MPPT) influences the perovskite surface in the first 24 hours of the ageing test. Interestingly, the effect of the light exposure induces structural modifications at the perovskite surface with the formation of $Cs_4PbBr_6$ phase without impacting on the structural properties of the bulk as confirmed by Photo Emission Spectroscopy (PES) and *insitu* XRD analysis. Finally, we found that IL addition further stabilized the device performance under light and thermal stress performing ISOS-L1, ISOS-D1 and ISOS-D2 ageing protocols.

**Results**

In this work, we developed a sequential deposition technique in order to fabricate $CsPbBr_3$ perovskite thin film by obtaining the perovskite conversion depositing CsBr precursor on $PbBr_2$-coated FTO/$TiO_2$ substrates. Notably, the CsBr solution is based on $H_2O$/ETOh solvent mixture without using harmful methanol solvent. 2-propanol is used as anti-solvent in order to remove unreacted CsBr precursor from the film surface. The $CsPbBr_3$ perovskite is fully converted using a single CsBr deposition and after annealing at 250°C for five minutes. In the $PbBr_2$ deposition, we incorporated $BMIMBF_4$ IL in $PbBr_2$ solution (**Figure 1A**) at different concentrations (5 µl/ml (IL5), 10 µl/ml (IL10), and 15 µl/ml (IL15) starting from a stock IL solution at 50ul/ml in DMSO. In **Figure 1B**, we presented the semitransparent PSC (ST-PSC) device stack consisting in FTO/c-$TiO_2$/$CsPbBr_3$/PTAA/ITO where PTAA is chosen for mitigating the sputtering damage occurred after RF-sputtering of the ITO electrode[36].

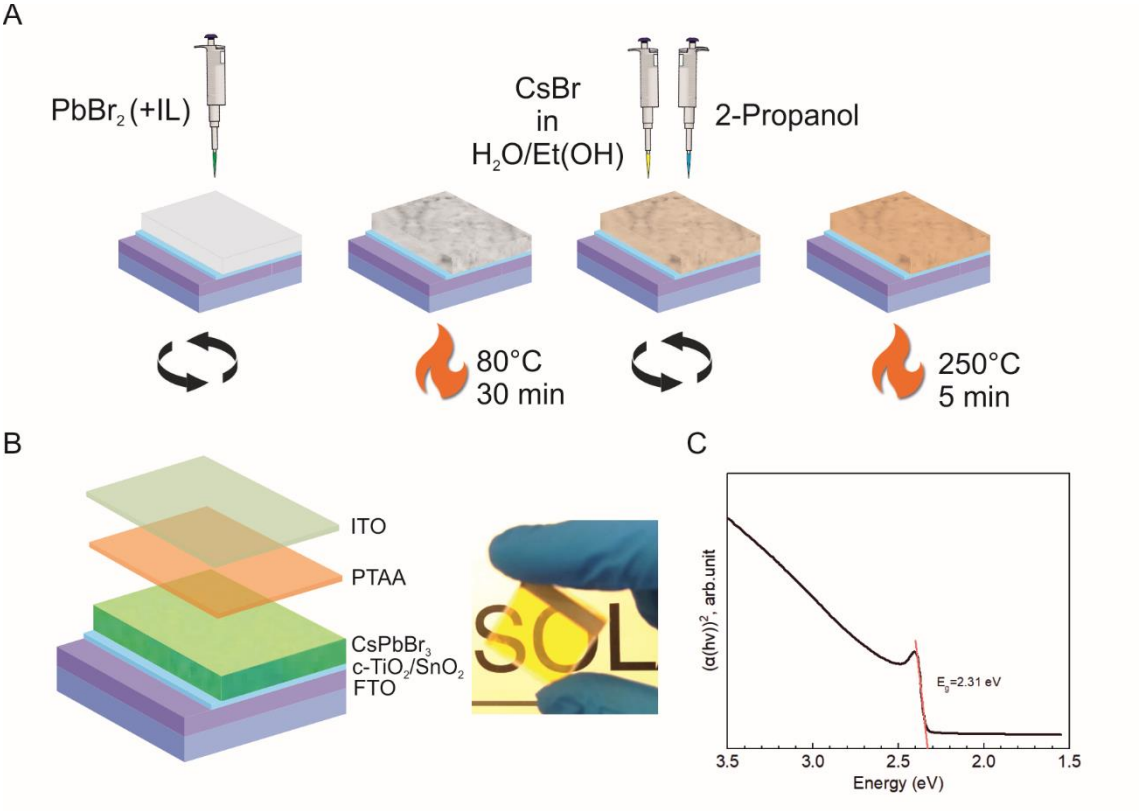


**Figure 1.** A) Schematic of the sequential deposition method adopted for $CsPbBr_3$ crystallization. It is mainly divided in two steps: First step: $PbBr_2$ (+IL) deposition and annealing at 80°C; Second Step: CsBr + Antisolvent Depositions and annealing at 250°C. B) Schematic and photo of the semitransparent device stack consisting in NIP architecture based on Glass/FTO/$TiO_2$/$CsPbBr_3$ (+IL)/PTAA/ITO C) Tauc plot calculated from the absorbance of Glass/$CsPbBr_3$ sample.

The $CsPbBr_3$ perovskite layer was deposited on glass substrate in order to measure the absorbance (**Figure S1**). The bandgap of the $CsPbBr_3$ perovskite is extracted by the TAUC plot shown in **Figure 1C** showing 2.31eV. The PV performance of a batch of representative cells varying the IL addition have been evaluated in comparison with reference device without IL. The box-plots of the PV parameters measured from a batch of six cells for each IL concentration are shown in **Figure S2.** The statistical results in terms of average and standard deviation are reported in **Table S1**. The results showed that PCE increases by adding IL with respect to the reference for all the tested concentrations reaching a maximum using IL10. The J-V characteristics of the best representative device for reference and IL10 showed (**Figure 2A**) PCE of 3.55% and 4.89%, respectively. In particular, we found remarkable increase of the FF and $V_{OC}$ passing from 56% to 66% and from 1.3V to 1.4V, respectively. Moreover, **Figure 2B** further confirms a slight $J_{SC}$ improvement using IL10 as confirmed from the comparison of the EQE spectrum passing from 4.9 mA/cm$^2$ to 5.1 mA/cm$^2$ (table S1). **Figure 2C** displays the transmittance spectra of the stack of REF and IL10 full devices. The AVT values achieved are 55.4% and 56.9% for the pristine and IL-treated devices, respectively. As

expected, the addition of IL does not alter the perovskite thickness, resulting in comparable AVT values.

With the aim of explaining the main difference between reference and IL samples, we performed XRD, Scanning Electron Microscopy (SEM) and Atomic Force Microscopy (AFM) analysis in order to grasp important information about structural and morphological changes. XRD analysis was performed upon fully ST-PSCs using the following architecture: Glass/FTO/$TiO_2$/$SnO_2$/$CsPbBr_3$ (+IL)/PTAA/ITO for reference and IL10 based devices (**Figure 2C**). The role of IL addition upon the structural properties of the 3D-$CsPbBr_3$ perovskite has been quantitative evaluated with respect the presence of competitive perovskite phases to $CsPbBr_3$ well known in literature such as $Cs_4PbBr_6$ and $CsPbBr_5$[25]. The substrate (Glass/FTO/$TiO_2$) is the same for both samples and labelled in figure according to FTO JCDD card nr: 00-041-1445. No ionic liquid contribution is detected nor is any PTAA signature, suggesting the polymer is amorphous, as expected. Monoclinic Cesium Lead Bromide $CsPbBr_3$ is well detected and reflections are labeled according to JCDD card nr: 00-018-0364 . $Cs_4PbBr_6$ is also detected, corresponding to h a rombohedral crystal system, the reflections are perfectly matching JCDD card nr: 01-073-2478. The beneficial role of the IL is attributed to the enhancement of the α-phase of the $CsPbBr_3$ perovskite, as confirmed by the quantitative analysis of XRD reflections reported in **Figure 2C**. Indeed, as reported in **Table S2**, overall crystallinity of the reference film is attributed as follows: 40% - $CsPbBr_3$ and 60% $Cs_4PbBr_6$, while with the addition of IL the crystallinity of the α-phase $CsPbBr_3$ is increased up to 50%.

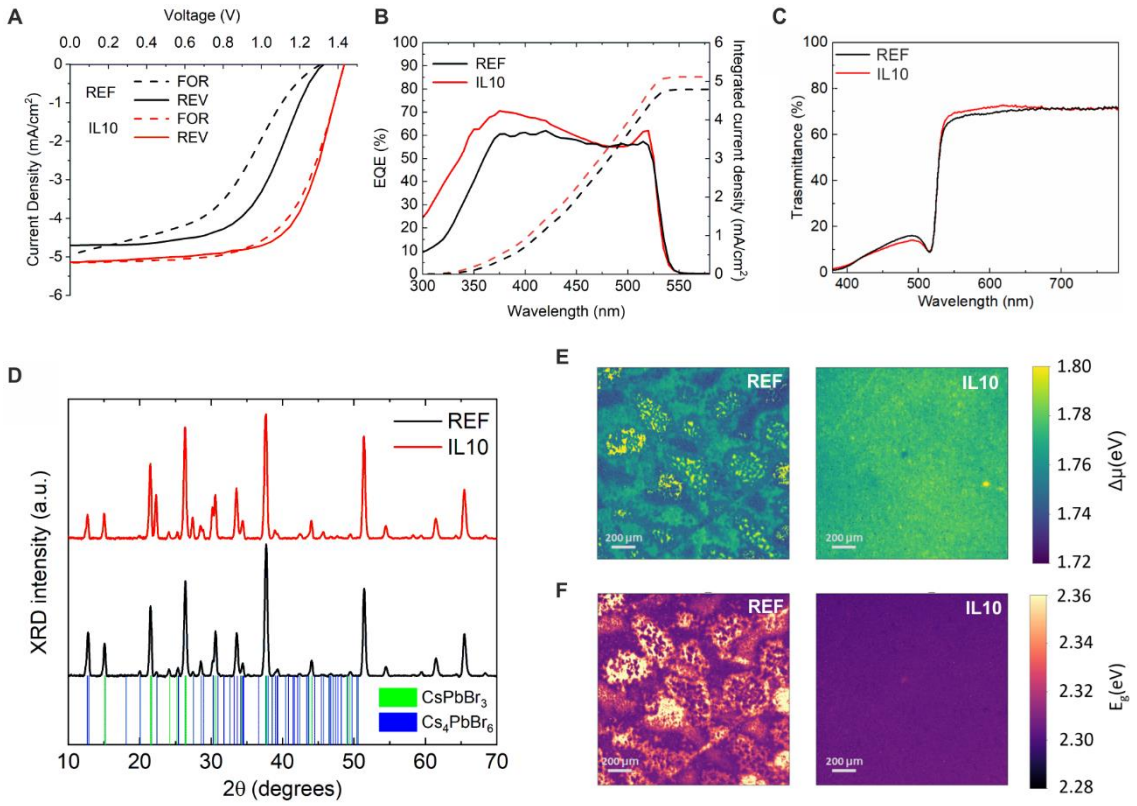


**Figure 2.** A) J-V characteristics of the pristine REF and IL10 devices measured under 1 Sun AM1.5G illumination condition under forward and reverse scan directions B) EQE spectra and Integrated current densities of REF and IL10 devices. C) Transmittance of the full stack devices (REF and IL10) including sputtered ITO electrode. AVT is calculated from 380 to 780 nm D) XRD performed on the pristine REF and IL10 devices; the green and blue columns refer to the theoretical XRD reflections of Monoclinic CsPbBr3 and Rhombohedral Cs4PbBr6 perovskite phases E) Quasi-Fermi Level Splitting (QFLS) and Energy bandgap maps of pristine REF and IL 10 CsPbBr3 thin films.

High-magnification SEM microscope images (**Figure S3A-B**) revealed minimal differences in grain size between REF and IL10 samples. However, low-magnification SEM images shown in **Figures S3C-D** clearly demonstrate that the IL10 sample exhibits better substrate coverage forming a pinhole free. Cross-sectional SEM image of the full stack of IL10 device shows $CsPbBr_3$ perovskite thickness of approximately 250-300 nm (**Figure S3E**).

To better understand the impact of ionic liquid on the optoelectronic properties of perovskite, we conducted multidimensional photoluminescence imaging. The perovskite thin films (reference and IL10) were deposited on glass and illuminated with a blue LED (405 nm) with a light intensity equivalent to 1 sun. We employed a pixel-to-pixel fitting process[16, 37 38] on absolutely calibrated PL spectra to derive key physical parameters such as the band gap ($E_g$) and the quasi-fermi level splitting (QFLS or $\Delta\mu$). **Figures 2E-F** present the QFLS and $E_g$ maps of the reference and IL-treated samples,

respectively. Whereas the untreated $CsPbBr_3$ exhibits an inhomogeneous layer with an average $E_g$ = 2.32 eV and $\Delta\mu$ = 1.76eV and a standard deviation of approximately 30 and 15 meV respectively, the introduction of ionic liquid leads to a homogenization of the perovskite film (**Table S3**). Specifically, for the IL-treated $CsPbBr_3$, a marginal statistical dispersion of approximately 5 meV is determined for both $E_g$ and QFLS. The correlation between $E_g$ and QFLS and their statistic distribution are depicted in **Figure S4**. This analysis confirms that the introduction of the ionic liquid has a beneficial impact on enhancing the quality of inorganic $CsPbBr_3$ thin films, notably improving sample homogeneity. These findings are consistent with the observed enhancements in device performance reaching higher Voc in IL-treated samples. In conclusion, the IL addition in the first step of perovskite deposition enhances the presence of the $CsPbBr_3$ phase in comparison to the other 0-D phase and improved the distribution and uniformity of the perovskite.

A crucial topic in PSC technology is the stability study of the structural and compositional properties of the perovskite absorbers upon continuous light exposure, heat and moisture stresses[39]. Here, we evaluated the shelf-life stability of the devices for 3000 hours when stored in dark at specific temperature (RT and 85°C) by following ISOS-D-1 and ISOS-D2 protocols, respectively. Both stability tests have been performed in air at moderate relative moisture levels without applying any encapsulation procedure. In ISOS-D-1 test, the device demonstrated impressive stability without showing any losses in PCE. In ISOS-D-2, the device retained 92.8% of the initial PCE after 3000 hours with not evident signs of degradation. Both tests confirm that ST-PSC made with IL-treated $CsPbBr_3$ perovskite and ITO electrode has a good potential in terms of environmental and thermal stability.

Furthermore, we performed a prolonged light soaking (ISOS-L-1) at 1 Sun illumination condition under operative conditions tracking the PCE at Maximum Power Point (MPP) using a Perturbe&Observe MPPT algorithm. As shown in **Figure 3C**, the prolonged light soaking test at MPP device shows promising stability achieved 200 hours. In the first 50 hours, the MPP-tracked PCE ($PCE_{MPP}$) remarkably increased, reaching a plateau for the entire duration of the test.

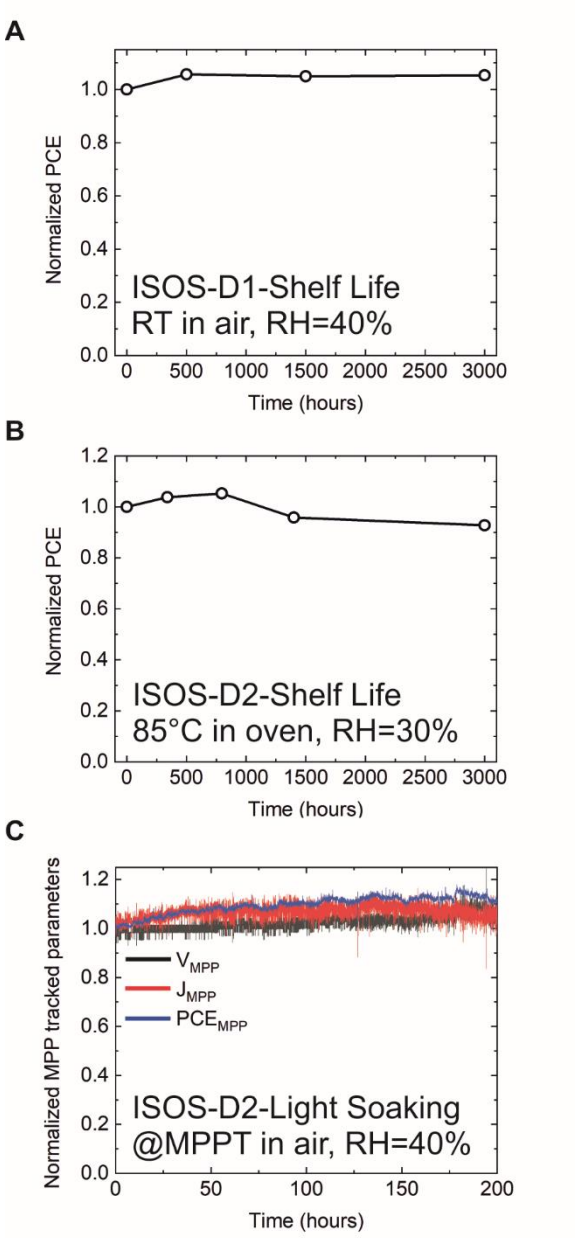


**Figure 3.** A-B) Shelf-life stability tests in dark storage at RT for ISOS-D-1 and 85°C for ISOS-D-2. C) Light soaking test made in air (ISOS-L-1) using MPPT algorithm. The illumination condition was settled at 1Sun using LED lamp. All stability tests have been performed in air at moderate relative moisture levels without applying any encapsulation procedure.

The evaluation of the stability in the first hours of the ISOS-L-1 is an interesting topic to analyze how the light exposure could induce remarkable changes in the bulk and at the interfaces between perovskite and the selective contacts[40]. In this scenario, the $CsPbBr_3$ system is an interesting case study to reveal the impact of the light exposure when the $CsPbBr_3$ phase coexist with the presence of competitive perovskite phases. With this aim, we performed several light soaking tests on a batch of $CsPbBr_3$ IL (IL10) based devices. Interestingly, we observed a relative increase of almost 10-15% in MPP tracked PCE during the first 24 hours of light soaking for all three IL10 devices (**Figure S5**).

During MPPT, the J-V characteristics were measured under forward and reverse scan directions to obtain information on PV parameters of the cells during the test. The J-V results showed a drastic increase of the FF, a constant $J_{SC}$ and a slight increase of the $V_{OC}$ values. From these results, we speculated that initial light exposure is not affecting the light harvesting properties of the perovskite in the bulk (no Jsc changes). The reasons behind this systematic behavior can be explained by changes at the interface between the perovskite and selective layers[41, 42].

**Figure 4A** shows the J-V characteristics before and after the light soaking at MPP showing the PV parameters reported in **Table S4**. To gain a better understanding of the effect of light soaking, we performed photoemission spectroscopy and *in situ* XRD analysis to reveals changes on composition and structural properties at the surface and/or in the bulk of the perovskite film.

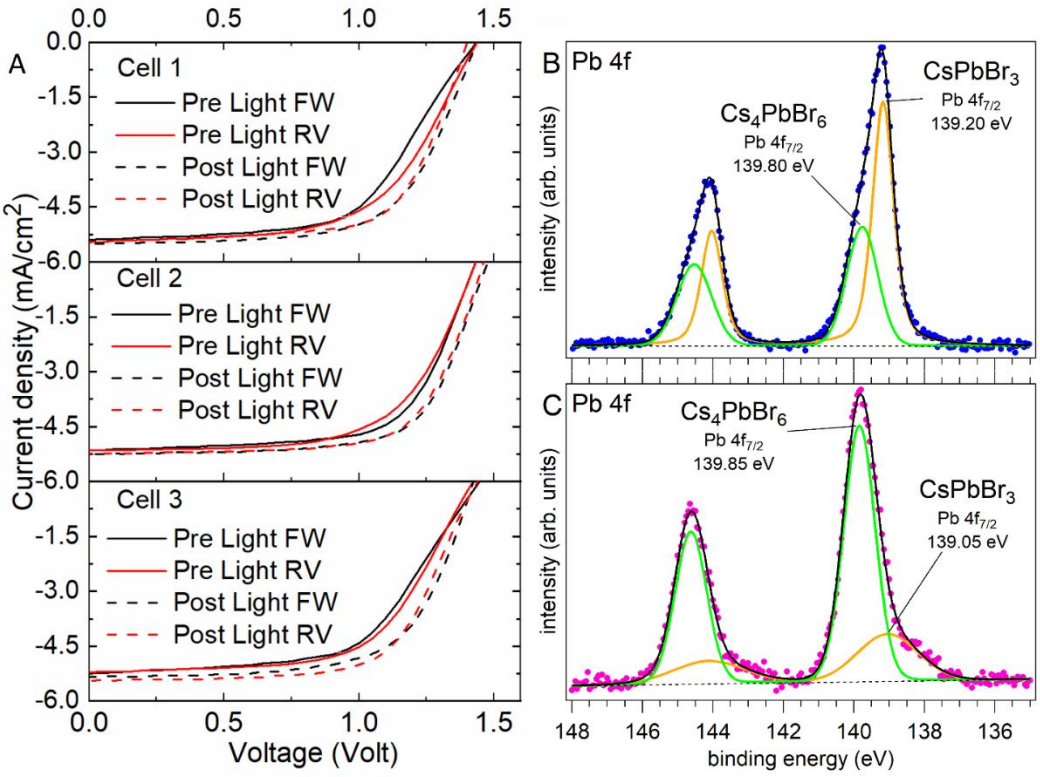


**Figure 4.** A) J-V characteristics pre and post light soaking at MPP for 24 hours. B) Pb 4f photoemission spectra of the perovskite film (B) before and (C) after light soaking. The orange and green line indicate the doublets assigned to $CsPbBr_3$ and $Cs_4PbBr_6$, respectively.

Photoemission spectroscopy with synchrotron radiation was used to monitor the chemical changes occurring in the near surface region of the perovskite layer upon light soaking. We collected Pb 4f, Cs 4d and Br 3d core level spectra with hν = 936 eV before and after light soaking (top and bottom row of **Figure S6**, respectively) and determined the areas of the corresponding peaks ($A_{Pb}$, $A_{Cs}$, $A_{Br}$). Both $A_{Cs}/A_{Pb}$ and $A_{Br}/A_{Pb}$ ratios increase after light soaking (from 0.46 to 0.52 for $A_{Cs}/A_{Pb}$, from 0.51 to 0.56 for $A_{Br}/A_{Pb}$). This indicates a higher surface concentration of Cs and Br in the perovskite film

after exposure to light. Notably, the position of the peaks in the bottom row spectra is shifted to higher binding energies by 0.35-0.50 eV with respect to the top row spectra, as highlighted by vertical dashed lines in **Figure S5**. To find the origin of this shift, we collected the Pb 4f spectra at hν = 270 eV, which provides much higher energy resolution than hν = 936 eV. The Pb 4f spectra before and after light soaking are reported in **Figures 4B-C**, respectively. The applied fitting procedure highlights the presence of two doublets in the Pb 4f spectra, with the Pb $4f_{7/2}$ components at about 139.20 and 139.85 eV. Evidently, the relative intensities of the two components reverse upon light soaking (from 1.40 to 0.35), thus explaining the apparent energy shift observed at hν = 936 eV. Because of the increased Cs and Br surface concentration derived from **Figure S6** and the coexistence of $CsPbBr_3$ and $Cs_4PbBr_6$ already reported for the perovskite film, we attribute the Pb 4f doublet at lower binding energy to $CsPbBr_3$ and Pb 4f doublet at higher binding energy to $Cs_4PbBr_6$. Overall, photoemission spectroscopy shows that the effect of light soaking is that $Cs_4PbBr_6$ tends to float on the surface of the perovskite film, thus forming a two-dimensional layer.

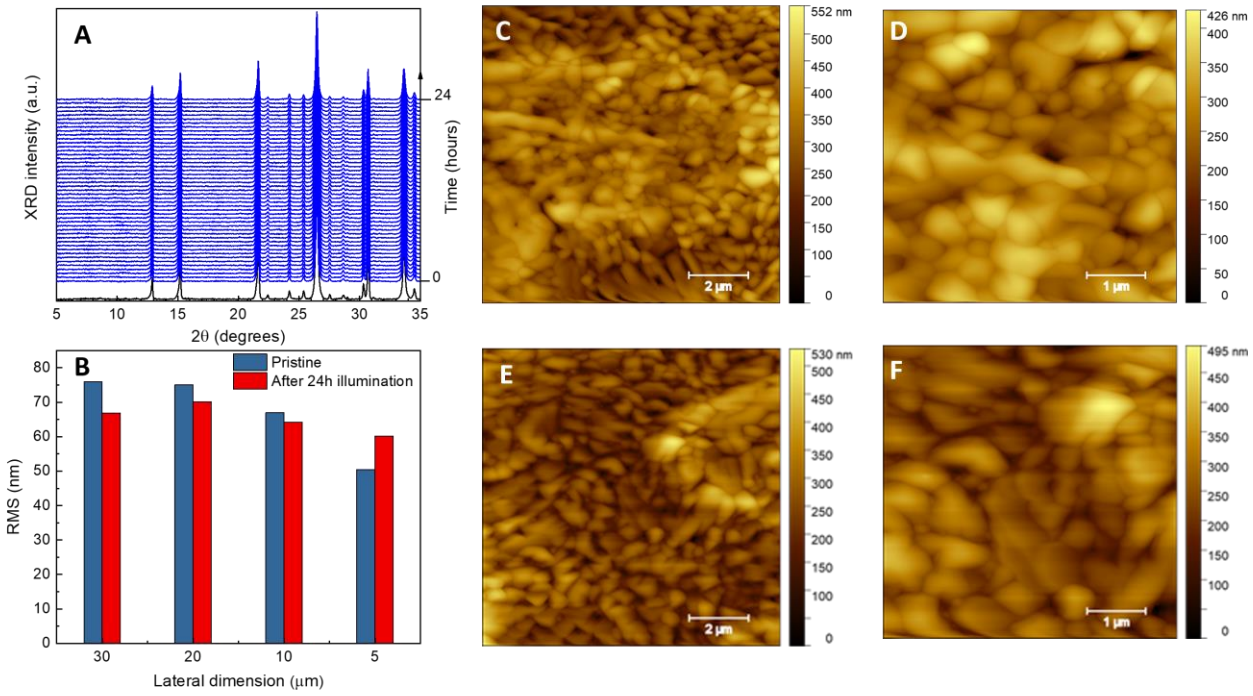


**Figure** 5 A) Time resolved XRD scan collected during 24h in-situ illumination of the perovskite layer. B) Root Mean Square (RMS) of the surface roughness acquired by Atomic Force Microscopy mapping of the perovskite surface prior and after 24h illumination at different lateral dimension of the AFM maps (5, 10, 20, 30 um); C-F AFM maps of the perovskite surface prior (4C-D) and after 24h illumination (E-F) acquired at two lateral dimensions (10 μm and 5 μm).

XRD analysis allowed to uncover that under light soaking the $CsPbBr_3$ phase remains stable without degrading when the intermediate sample is considered. Indeed, starting from the pristine material with a 63% contribution attributed to $CsPbBr_3$ phase (**figure S7**), no further evolution of the two phases was observed upon illumination, as reported in **Figure 5A**. The RMS values evaluated before and after illumination are in fact essentially comparable (**Figure 5B**), with average values of 67 ± 12 nm and 65 ± 4 nm for the pristine and illuminated film, respectively. Furthermore, from the AFM analysis in **Figure 5C-F**, no evident morphological changes were detected after illumination.

Differently, upon continuous illumination of the complete cell, the involved phases evolve toward an equilibrium condition, with a predominant contribution attributed to the $CsPbBr_3$ α-phase as shown in **Figure S8** reporting the XRD patterns of the device before and after light soaking, comparable to the value measured for the intermediate pristine device reported in **Figure 4**. We speculate that a surface $Cs_4PbBr_6$ layer is obtained[43] after light exposure which can passivate defects and protect the bulk layer (**Figure 4B**). Meanwhile, the α-phase in the bulk structure remains constant, with no decrease in $J_{SC}$ (**Figure 4A**). However, passivation occurs, leading to an increase in $V_{OC}$ and FF (**Figure 4A and table S3**). A progressive increase in PCE reaching values up to 5.3% is detectable after 24 hours of light exposure. The champion ST-PSC achieved a maximum PCE of 6.1 % with a remarkable $V_{OC}$ of 1.5 V, a full stack AVT of 58% for a final LUE of 3.53%.

## Conclusion

In this paper, we demonstrate the development of ST-PSCs based on $CsPbBr_3$ using sequential deposition for application in BIPV field. The sequential deposition implies the $PbBr_2$ deposition followed by a single CsBr deposition to obtain pure α-phase perovskite when annealed at elevated temperature. Unfortunately, we found the presence of competitive $Cs_4PbBr_6$ phase using pristine $PbBr_2$ thin films that can drastically affect the uniformity of the obtained perovskite films impacting on PV performance. To solve this issue, low content of BMIM-$BF_4$ ionic liquid were added in the $PbBr_2$ solution demonstrating beneficial effect on performance and stability of ST-PSC devices. After the optimization of the ionic liquid addition, we found that 10 µl/ml was the best concentration to achieve good coverage and homogeneous $CsPbBr_3$ film as further confirmed from SEM and PL mapping. Furthermore, lower content of competitive $Cs_4PbBr_6$ phase in the bulk has been detected as demonstrated from XRD analysis. On IL-based ST-PSC devices, we performed several stability protocols showing promising results under light exposure, dry heat and shelf-life condition. Regarding light exposure, we found a remarkable increase (+10-15% absolute) of the PV performance after 24 hours. This behavior inspired us to collect more data regarding the structural perovskite and composition changes at the bulk and the surface of the $CsPbBr_3$ film performing *insitu* XRD and PES

analyses upon illumination. Interestingly, with PES analysis, we found that only the perovskite surface changed. PES showed a higher surface concentration of Cs and Br in the perovskite film after light exposure due to the formation of a two-dimensional layer of $Cs_4PbBr_6$ on the surface of the perovskite film. We speculated that it acts as a passivating agent at the surface of the perovskite leading to an increase of Voc and FF values and then to the overall PCE. Finally, the combination of the effect of the IL addition and of the light exposure permit us the development of a ST-PSC device with champion PCE of 6.1%, AVT of 58% leading to a LUE of 3.53%. These findings can be useful for exploitation of the $CsPbBr_3$ perovskite in BIPV and in another application fields such as x-ray/particle detection.

## Materials and Methods

*Device fabrication*

Conductive FTO (7 Ω/□) substrates from Pilkington, with a square shape of 2.5 x 2.5 $cm^2$, were first etched with a P1 process using a ps-laser (Wophotonics, Yb:KGW, λ = 355 nm, 5 ps, pulsed at 2000 kHz) to electrically separate the conductive surface. Subsequently, they were mechanically washed with a 2% soap/water mixture (Hellmanex). The substrates were then rinsed in an ultrasonic bath at 40°C in distilled water and in a second ultrasonic bath in isopropanol for 10 minutes. To remove organic compounds, the cleaned substrates underwent UV/$O_3$ treatment with a PSD Pro Series Digital UV Ozone System (Novascan). A solution of 0.16 M $Ti(AcAc)_2$ and 0.4 M AcAc in EtOH was prepared to deposit the compact $TiO_2$ as the electron transport layer (ETL) using the spray pyrolysis technique. The ETL deposition occurred through air as the gas carrier at a pressure of 1.6 bar and a nozzle angle of about 45°, with 8-10 spray cycles (one every 10 seconds) when the hot plate reached 460 °C. The hot plate was maintained at 460°C for 10 minutes and then the temperature was decreased. $SnO_2$ nanoparticle-based ink at 1:20 v/v in deionized water is deposited by spin coating at 4000 rpm for 20 s followed by an annealing step made at 120 °C for 20 minutes. $CsPbBr_3$ perovskite was grown through a sequential deposition. $PbBr_2$ solution (1M in DMSO) and CsBr (250mg/ml in water/ethanol (9:1 in vv) solvent mixture) were prepared. A stock solution of BMIM-BF4 (1-Butyl-3-methylimidazolium tetrafluoroborate) IL at 40 µl/ml in DMSO was prepared the day before the deposition. The perovskite film was deposited using the sequential deposition method (Figure 1). 80 µl of $PbBr_2$ was dropped on hot substrates at 60°C and then spin coated at 4000 rpm for 20 seconds and allowed to dry for 30 minutes at 80°C in an $N_2$ atmosphere. For IL doped $PbBr_2$ layers, IL stock solution was added to the $PbBr_2$ solution in different amounts: 5 µl/ml, 10 µl/ml, 15 µl/ml, and 20 µl/ml prior the deposition.

In an ambient atmosphere, 100 µl of CsBr was dropped dynamically on hot substrates (60°C) while spin coated at 4000 rpm for 30 seconds. After 20 seconds from the start of spinning, 200 µl of isopropanol was added to remove the excess, followed by 5 minutes of sintering at 250 °C. 10 mg of PTAA powder was dissolved in 1 ml of toluene solvent and doped with TBP (10µl/ml) and Li-TFSI (5µl/ml, stock solution: 170mg/ml in acetonitrile). The PTAA film was deposited by spin coating at 4000 rpm for 20 seconds. An industrial in-line magnetron sputtering (KENOSISTEC S.R.L., KS 400 In-Line) was used to deposit low-temperature ITO at $1.1 \cdot 10^{-3}$ mBar and 90W RF power. During the ITO deposition, inert Ar gas was purged in the chamber (40sccm) to activate the Ar+ plasma. The sample holder was moved below the ITO cathode with a speed of 120 cm/min for 200 cycles to achieve a thickness of 220 nm.

*Device Characterization*

J-V curves and PV parameters of devices were detected by a Class-A Sun Simulator (ABET 2000) furnished with an AM1.5G filter (ABET). For calibrating the sun simulator, a Si-based reference cell (RR-226-O, RERA Solutions) was utilized. Arkeo platform (Cicci Research S.r.l.) was used for J-V data acquisition under forward and reverse voltage scan modes, using a voltage step of 50 mV $s^{-1}$ and a voltage scan rate of 300 mV $s^{-1}$.

An UV-vis spectrophotometer (Shimadzu UV-2550) equipped with an integrated sphere was used for the acquisition of transmittance spectra of the transparent devices. The AVT values of transparent PSCs were calculated according to the method reported in the ISO 9050:2003 standard using the following equation: AVT=[∫ 380^780 〖D(λ)〗 ×T(λ)×V(λ)dλ]⁄ [∫ 380^780 〖D(λ)〗 ×V(λ)dλ], in which D(y) is the incident light spectral distribution, V(y) is the sensitivity factor of the human eye, and T(λ) is the transmittance. An “Arkeo” light soaker (from CICCI research) was used for the light soaking test (CICCI Research).

X-Ray Diffraction (XRD): A Panalytical Empyrean Diffractometer was used to perform X-ray diffraction measurements in reflection mode. The k Alpha fluorescence lines (K-Alpha1 [Å] = 1,54060; K-Alpha2 [Å] = 1,54443) of a Cu-anode were selected as impinging radiation and a solid-state hybrid Pix’cel 3D detector, working in 1D linear mode, accomplished the detection. High angle XRD measurements were collected in the $10° < 2\theta < 70°$ angular range and Bragg Brentano configuration was adopted focusing the impinging beam with fixed divergent slits (1/4°-1/2°). Low angle acquisitions ($2.5° < 2\theta < 20°$) were obtained narrowing down the slit dimensions to (1/32°-1/16°) to detect 2D structures.

Hyperspectral photoluminescence imaging: The hyperspectral imaging (HI) system recorded a luminescence intensity signal along three dimensions (x,y,λ). The set-up was composed of a home-built microscope with Thorlabs optomechanical elements, a 2D bandpass filtering system from the company PhotonEtc with 2 nm resolution, and a 1Mpix silicon-based CCD camera PCO1300. The sample was illuminated (λ = 405 nm) through an infinity-corrected 10x Olympus objective with a numerical aperture of 0.25, and the luminescence was collected through the same objective. The excitation beam and luminescence signals are separated with the appropriate Thorlabs dichroic beam splitter (DMLP425) and Semrock spectral filter (long pass 450 nm cut-off wavelength). The 2D luminescence signal was corrected for each pixel of the sensor from the spectral transmissions along all the optical paths, from the read noise and dark current noise of the camera. The acquisitions were performed in an air atmosphere, at 40% RH and at the temperature of 25 °C.

Photoemission spectroscopy data were collected at the VUV-Photoemission beamline of the Elettra synchrotron radiation facility (Trieste, Italy) using photon energy of hν = 936 eV High resolution spectra of the Pb4f core levels were measured also at hν = 270 eV to distinguish spectroscopically the $CsPbBr_3$ and $Cs_4PbBr_6$ phases.


1. M. A. Green, E. D. Dunlop, M. Yoshita, N. Kopidakis, K. Bothe, G. Siefer and X. Hao, *Progress in Photovoltaics: Research and Applications*, 2023, **31**, 651-663.
2. D. Li, P. Wu and F. Zhang, *Joule*, 2023, **7**, 628-630.
3. Y. Zou, W. Yu, H. Guo, Q. Li, X. Li, L. Li, Y. Liu, H. Wang, Z. Tang, S. Yang, Y. Chen, B. Qu, Y. Gao, Z. Chen, S. Wang, D. Zhang, Y. Chen, Q. Chen, S. M. Zakeeruddin, Y. Peng, H. Zhou, Q. Gong, M. Wei, M. Grätzel and L. Xiao, *Science*, 2024, **385**, 161-167.
4. M. Chen, T. Niu, L. Chao, X. Duan, J. Wang, T. Pan, Y. Li, J. Zhang, C. Wang, B. Ren, L. Guo, M. Hatamvand, J. Zhang, Q. Guo, Y. Xia, X. Gao and Y. Chen, *Energy & Environmental Science*, 2024, **17**, 3375-3383.
5. Z. Huang, Y. Bai, X. Huang, J. Li, Y. Wu, Y. Chen, K. Li, X. Niu, N. Li, G. Liu, Y. Zhang, H. Zai, Q. Chen, T. Lei, L. Wang and H. Zhou, *Nature*, 2023, **623**, 531-537.
6. Y. Lin, W. Yang, H. Gu, F. Du, J. Liao, D. Yu, J. Xia, H. Wang, S. Yang, G. Fang and C. Liang, *Advanced Materials*, 2024, **36**, 2405684.
7. Z. Cheng, M. Zhang, Y. Zhang, W. Qi, Z. Wang, B. Liu and D. Di, *Nano Energy*, 2024, **127**, 109708.
8. J. Lim, N.-G. Park, S. Il Seok and M. Saliba, *Energy & Environmental Science*, 2024, **17**, 4390-4425.
9. Z. Zhou, Z. Yuan, Z. Yin, Q. Xue, N. Li and F. Huang, *Green Energy & Environment*, 2024, **9**, 992-1015.
10. P. Kumar, S. You and A. Vomiero, *Advanced Energy Materials*, 2023, **13**, 2301555.
11. J. Lou, J. Feng, S. Liu and Y. Qin, *Solar RRL*, 2023, **7**, 2200708.
12. C. J. Traverse, R. Pandey, M. C. Barr and R. R. Lunt, *Nature Energy*, 2017, **2**, 849-860.
13. C. O. Ramírez Quiroz, I. Levchuk, C. Bronnbauer, M. Salvador, K. Forberich, T. Heumüller, Y. Hou, P. Schweizer, E. Spiecker and C. J. Brabec, *Journal of Materials Chemistry A*, 2015, **3**, 24071-24081.
14. E. Della Gaspera, Y. Peng, Q. Hou, L. Spiccia, U. Bach, J. J. Jasieniak and Y.-B. Cheng, *Nano Energy*, 2015, **13**, 249-257.

15. L. Yuan, Z. Wang, R. Duan, P. Huang, K. Zhang, Q. Chen, N. K. Allam, Y. Zhou, B. Song and Y. Li, *Journal of Materials Chemistry A*, 2018, **6**, 19696-19702.
16. F. Jafarzadeh, L. A. Castriotta, M. Legrand, D. Ory, S. Cacovich, Z. Skafi, J. Barichello, F. De Rossi, F. Di Giacomo, A. Di Carlo, T. Brown, F. Brunetti and F. Matteocci, *ACS Applied Materials & Interfaces*, 2024, **16**, 17607-17616.
17. J. García Cerrillo, A. Distler, F. Matteocci, K. Forberich, M. Wagner, R. Basu, L. A. Castriotta, F. Jafarzadeh, F. Brunetti, F. Yang, N. Li, A. N. Corpus-Mendoza, A. Di Carlo, C. J. Brabec and H.-J. Egelhaaf, *Solar RRL*, 2024, **8**, 2300767.
18. J. Barichello, D. Di Girolamo, E. Nonni, B. Paci, A. Generosi, M. Kim, A. Levtchenko, S. Cacovich, A. Di Carlo and F. Matteocci, *Solar RRL*, 2023, **7**, 2200739.
19. F. Matteocci, D. Rossi, L. A. Castriotta, D. Ory, S. Mejaouri, M. A. der Maur, F. Sauvage, S. Cacovich and A. Di Carlo, *Nano Energy*, 2022, **101**, 107560.
20. D. Di Girolamo, G. Vidon, J. Barichello, F. Di Giacomo, F. Jafarzadeh, B. Paci, A. Generosi, M. Kim, L. A. Castriotta, M. Frégnaux, J.-F. Guillemoles, F. Brunetti, P. Schulz, D. Ory, S. Cacovich, A. Di Carlo and F. Matteocci, *Advanced Energy Materials*, **n/a**, 2400663.
21. X.-Y. Li, Q. Sun, Y.-M. Xie and M.-K. Fung, *Advanced Energy and Sustainability Research*, 2024, **5**, 2300263.
22. J. Shi, M. Wang, Z. Da, C. Zhang, J. Wang, Y. Ding, Y. Xu and N. V. Gaponenko, *Nanoscale*, 2023, **15**, 11190-11198.
23. V. G. V. Dutt, S. Akhil, R. Singh, M. Palabathuni and N. Mishra, *The Journal of Physical Chemistry C*, 2022, **126**, 9502-9508.
24. D. Di Girolamo, M. I. Dar, D. Dini, L. Gontrani, R. Caminiti, A. Mattoni, M. Graetzel and S. Meloni, *Journal of Materials Chemistry A*, 2019, **7**, 12292-12302.
25. Z.-L. Yu, Y.-Q. Zhao, Q. Wan, B. Liu, J.-L. Yang and M.-Q. Cai, *The Journal of Physical Chemistry C*, 2020, **124**, 23052-23058.
26. S. Ullah, J. Wang, P. Yang, L. Liu, S.-E. Yang, T. Xia, H. Guo and Y. Chen, *Materials Advances*, 2021, **2**, 646-683.
27. G. Che, X. Wang, C. Cui, B. Pang, X. Wang, H. Dong, J. Feng, L. Yu and L. Dong, *Journal of Alloys and Compounds*, 2023, **969**, 172423.
28. X. Cao, G. Zhang, L. Jiang, Y. Cai, Y. Gao, W. Yang, X. He, Q. Zeng, G. Xing, Y. Jia and J. Wei, *ACS Applied Materials & Interfaces*, 2020, **12**, 5925-5931.
29. H. Yuan, Y. Zhao, J. Duan, Y. Wang, X. Yang and Q. Tang, *Journal of Materials Chemistry A*, 2018, **6**, 24324-24329.
30. G. Tong, T. Chen, H. Li, L. Qiu, Z. Liu, Y. Dang, W. Song, L. K. Ono, Y. Jiang and Y. Qi, *Nano Energy*, 2019, **65**, 104015.
31. S. Panigrahi, S. Jana, T. Calmeiro, D. Nunes, R. Martins and E. Fortunato, *ACS Nano*, 2017, **11**, 10214-10221.
32. Z.-J. Zhou, Y.-Q. Deng, P.-P. Zhang, D.-X. Kou, W.-H. Zhou, Y.-N. Meng, S.-J. Yuan and S.-X. Wu, *Solar RRL*, 2019, **3**, 1800354.
33. X. Jiang, C. Geng, X. Yu, J. Pan, H. Zheng, C. Liang, B. Li, F. Long, L. Han, Y.-B. Cheng and Y. Peng, *ACS Applied Materials & Interfaces*, 2024, **16**, 19039-19047.
34. J. Yang, J. Hu, W. Zhang, H. Han, Y. Chen and Y. Hu, *Journal of Energy Chemistry*, 2023, **77**, 157-171.
35. W. Zhang, X. Liu, B. He, Z. Gong, J. Zhu, Y. Ding, H. Chen and Q. Tang, *ACS Applied Materials & Interfaces*, 2020, **12**, 4540-4548.
36. E. Lamanna, F. Matteocci, E. Calabrò, L. Serenelli, E. Salza, L. Martini, F. Menchini, M. Izzi, A. Agresti, S. Pescetelli, S. Bellani, A. E. Del Río Castillo, F. Bonaccorso, M. Tucci and A. Di Carlo, *Joule*, 2020, **4**, 865-881.
37. S. Cacovich, G. Vidon, M. Degani, M. Legrand, L. Gouda, J.-B. Puel, Y. Vaynzof, J.-F. Guillemoles, D. Ory and G. Grancini, *Nature Communications*, 2022, **13**, 2868.
38. J. K. Katahara and H. W. Hillhouse, *Journal of Applied Physics*, 2014, **116**.
39. M. V. Khenkin, E. A. Katz, A. Abate, G. Bardizza, J. J. Berry, C. Brabec, F. Brunetti, V. Bulović, Q. Burlingame, A. Di Carlo, R. Cheacharoen, Y.-B. Cheng, A. Colsmann, S. Cros, K. Domanski, M. Dusza, C. J. Fell, S. R. Forrest, Y. Galagan, D. Di Girolamo, M. Grätzel, A. Hagfeldt, E. von Hauff, H. Hoppe, J.

Kettle, H. Köbler, M. S. Leite, S. Liu, Y.-L. Loo, J. M. Luther, C.-Q. Ma, M. Madsen, M. Manceau, M. Matheron, M. McGehee, R. Meitzner, M. K. Nazeeruddin, A. F. Nogueira, Ç. Odabaşı, A. Osherov, N.-G. Park, M. O. Reese, F. De Rossi, M. Saliba, U. S. Schubert, H. J. Snaith, S. D. Stranks, W. Tress, P. A. Troshin, V. Turkovic, S. Veenstra, I. Visoly-Fisher, A. Walsh, T. Watson, H. Xie, R. Yıldırım, S. M. Zakeeruddin, K. Zhu and M. Lira-Cantu, *Nature Energy*, 2020, **5**, 35-49.

40. L. Lin, L. Yang, G. Du, X. Li, Y.-n. Li, J. Deng, K. Wei and J. Zhang, *ACS Applied Energy Materials*, 2023, **6**, 10303-10318.
41. J. Hu, L. Gouda, A. Kama, S. Tirosh and R. Gottesman, *ACS Applied Energy Materials*, 2019, **2**, 3013-3016.
42. X. Yang, J. Jiang, C. Xu, P. Ji, W. Tang, L. Ma, H. Cai, F. Zhang and X. Wu, *ACS Applied Energy Materials*, 2022, **5**, 5603-5609.
43. F. A. La Porta and S. Masi, *Nanomanufacturing*, 2021, **1**, 67-74.